HIPPOCAMPUS 26:1593–1607 (2016)

Spatial Coding and Physiological Properties of Hippocampal Neurons in the Cornu Ammonis Subregions

Azahara Oliva,[1] Antonio Fernández-Ruiz,[1] György Buzsáki,[2,3] and Antal Berényi[1,2]*

ABSTRACT: It is well-established that the feed-forward connected main hippocampal areas, CA3, CA2, and CA1 work cooperatively during spatial navigation and memory. These areas are similar in terms of the prevalent types of neurons; however, they display different spatial coding and oscillatory dynamics. Understanding the temporal dynamics of these operations requires simultaneous recordings from these regions. However, simultaneous recordings from multiple regions and subregions in behaving animals have become possible only recently. We performed large-scale silicon probe recordings simultaneously spanning across all layers of CA1, CA2, and CA3 regions in rats during spatial navigation and sleep and compared their behavior-dependent spiking, oscillatory dynamics and functional connectivity. The accuracy of place cell spatial coding increased progressively from distal to proximal CA1, suddenly dropped in CA2, and increased again from CA3a toward CA3c. These variations can be attributed in part to the different entorhinal inputs to each subregions, and the differences in theta modulation of CA1, CA2, and CA3 neurons. We also found that neurons in the subregions showed differences in theta modulation, phase precession, state-dependent changes in firing rates and functional connectivity among neurons of these regions. Our results indicate that a combination of intrinsic properties together with distinct intra- and extra-hippocampal inputs may account for the subregion-specific modulation of spiking dynamics and spatial tuning of neurons during behavior. © 2016 Wiley Periodicals, Inc.

KEY WORDS: electrophysiology; place field; phase precession; deep vs. superficial; CA regions

INTRODUCTION

The mammalian hippocampal formation has received strong attention, largely because of its key role in spatial navigation (O'Keefe and Dostrovsky, 1971, McNaughton et al., 1996) and several aspects of memory formation, storage and recall (Squire, 1992, Eichenbaum et al., 1999, Vinogradova, 2001). The hippocampus proper (Cornu Ammonis) is divided into three different subregions named CA1, CA2, and CA3, based on their anatomical and molecular features (Lorente de Nó, 1947, Amaral and Witter, 1989, Amaral and Lavenex, 2007, Cembrowski et al., 2016, Dudek et al., 2016), and have been attributed with different functional roles (McNaughton and Morris, 1987, Rolls and Kesner, 2006, Leutgeb and Leutgeb, 2007, Knierim and Neunuebel, 2016). The principal (pyramidal) cells in these areas share many morphological and biophysical properties (Spruston et al., 1995a,b; Spruston, 2008). However, cells from these subregions also exhibit different firing patterns under several behavioral states, environmental manipulations or task demands (Lee et al., 2004a,b, Leutgeb et al., 2004, Mizuseki et al., 2012, Mankin et al., 2015, Kay et al., 2016).

The extensive recurrent collateral system of CA3 distinguishes this region as an autoassociative network performing pattern completion computations during memory retrieval (Wallenstein et al., 1998; Neunuebel and Knierim, 2014). On the other hand, CA1, the output region of the hippocampus, has a feed-forward organization with limited recurrent connectivity (Witter et al., 2000), and has been proposed to act as a feature integrator of the incoming information from its two main inputs: the CA3 and entorhinal cortex (EC) (Bittner et al., 2015). The smaller CA2 region has been traditionally neglected in terms of assignment of a distinct role, although several recent reports showed unique physiological properties of this region (Hitti and Siegelbaum, 2014; Kohara et al., 2014; Carstens et al., 2016; Dudek et al., 2016; Oliva et al., 2016). Recently a role has been proposed for CA2 in temporal encoding, through which CA2 firing variability over time would provide a temporal context to CA1 to differentiate between similar events (Mankin

[1] **MTA-SZTE 'Momentum' Oscillatory Neuronal Networks Research Group, Department of Physiology, University of Szeged, Szeged, Hungary;** [2] **New York University Neuroscience Institute, New York, New York;** [3] **Center for Neural Science, New York University, New York, New York**

Grant sponsor: EU-FP7-ERC-2013-Starting Grant; Grant number: 337075; Grant sponsor: "Momentum" Program of the Hungarian Academy of Sciences; Grant number: LP2013-62/2013; Grant sponsor: National Institute of Health; Grant numbers: NIHMH54671, MH107396, NS 090583; Grant sponsor: the Simons Foundation, EMBO and Marie Curie Actions; Grant number: ALTF 147-2015.

Author contribution: The experiments were conceived and designed by all authors. Recordings were per-formed by A.O., A.F.R., and A.B. Data analysis and immunohistological characterizations were performed by A.O. and A.F.R. The article was written by all authors.

*Correspondence to: Antal Berényi, MTA-SZTE 'Momentum' Oscillatory Neuronal Networks Research Group, Department of Physiology, University of Szeged, 10 Dom sqr., Szeged, H-6720, Hungary.
E-mail: drberenyi@gmail.com

Accepted for publication 9 September 2016.
DOI 10.1002/hipo.22659
Published online 20 September 2016 in Wiley Online Library (wileyonlinelibrary.com).

et al., 2015). Also, the CA2 region was highlighted recently in the encoding of the spatial position during immobility periods (Kay et al., 2016) and in initiating sharp-wave ripple events (Oliva et al., 2016).

Another important source of functional variability is the inhomogeneity of these regions since the principal cells' physiological properties, connectivity and functional roles vary along the transverse axis within each region. The proximal pole of CA1 (closer to the CA2 border) is innervated by axons from medial entorhinal cortex (MEC), while the distal pole is innervated by those from lateral entorhinal cortex (LEC) (Tamamaki et al., 1988; Witter et al., 2000). These projections have been found to carry information about different modalities (Hargreaves et al., 2005; Deshmukh and Knierim, 2011), and corresponding functional differences have been observed along this axis of CA1, with better spatial coding in its proximal part (Henriksen et al., 2010) and stronger responses to non-spatial stimuli in its distal pole (Burke et al., 2011; Igarashi et al., 2014). Connectivity also changes in CA3 from its proximal part (CA3c, closer to the dentate gyrus), intermediate (CA3b) to its distal pole (CA3a, closer to CA2). CA3c has stronger connections with the CA1 region and is relatively more influenced by perforant path information (which is first processed in the dentate gyrus), while CA3a has the strongest recurrent connectivity and receive the entorhinal information from layer II entorhinal axons both directly via monosynaptic connections, and disynaptically through the dentate gyrus (Li et al., 1994; Ishizuka et al., 1995). Analogous to CA1, spatial coding properties have been found to gradually change along the CA3 transverse axis (Lee et al., 2015; Lu et al., 2015).

In addition, the deep and superficial sublayers of CA1 have been proposed to constitute two types of neurons, with different connectivity, spiking and oscillatory properties and possibly specialized functional roles (Bannister and Larkman, 1995; Mizuseki et al., 2011; Valero et al., 2015; Danielson et al., 2016). The presence of any similar functional difference between the deep/superficial sublayers of the CA2 and CA3 regions has not been investigated.

The distribution of intrahippocampal connections between CA3 and CA1 regions show a unique topography: CA3c pyramidal cells project more strongly to distal portions of CA1 whereas fibers arising from cells located in CA3a subregion terminate more densely in proximal CA1 (Ishizuka et al., 1990, Li et al., 1994). This selective innervation also implies the possibility of transmitting different information across adjacent segments of each region. Although anatomical data are available about intrahippocampal axonal connections (Ishizuka et al., 1990, Witter et al., 2000), simultaneous recordings are required to examine how functional connectivity across hippocampal subregions contribute to information processing.

In addition to the intrinsic cellular properties, intrahippocampal connectivity and functional organization are factors that contribute to the observed gross functional differences of CA1, CA2, and CA3 regions during behavior. Previous studies investigated these regions individually, or at best, compared only two regions simultaneously (Jarsky et al., 2008, Valero et al., 2015). Studying each region separately in different animals and different laboratories with heterogeneous methods inevitably leads to large variability and numerous animals are needed to compare the individual observations quantitatively. Here we utilize the advantage of state-of-the-art large-scale silicon probe technology and set out to simultaneously record all subregions of CA1, CA2, and CA3 in behaving rats. We provide a comprehensive comparison of the physiological and functional differences along the anatomical subdivisions of hippocampal transverse axis.

MATERIALS AND METHODS

Surgery and Recordings

Surgery and recordings were performed in the Department of Physiology, Faculty of Medicine, University of Szeged and the Neuroscience Institute, Langone Medical Center of the New York University. All experiments were performed in accordance with European Union guidelines (2003/65/CE) and the National Institutes of Health Guidelines for the Care and Use of Animal Research and were approved by the Albert Szent-Györgyi Medical and Pharmaceutical Center of the University of Szeged and the Animal Care and Use Committee of New York University Medical Center.

Eight male rats (Long-Evans, 3–5 months old) were included in this study. Electrode fabrication and implantation surgery were discussed in detail earlier (Berenyi et al., 2014). Briefly, animals were anesthetized with isoflurane anesthesia and one or several craniotomies were created under stereotaxical guidance. Eight-shank, 256-site silicon-probes (NeuroNexus, Ann-Arbor, MI), with 300 μm inter-shank spacing, 32 electrode sites per shank separated vertically by 50 μm were implanted along the transverse axis of the dorsal hippocampus. Silicon probes were mounted on custom-made micro-drives to allow their precise vertical movement after implantation. To prevent the intraoperative damaging of the hippocampus, the probes were inserted above the target region and the micro-drives were attached to the skull with dental cement. The craniotomies were sealed with sterile wax. Two stainless steel screws were drilled bilaterally over the cerebellum served as ground and reference (ipsi- and contralateral, respectively) for the recordings. Several additional screws were drilled into the skull and covered with dental cement to strengthen the implant. Finally, a copper mesh was attached to the skull with dental cement and connected to the ground screw to act as a Faraday cage preventing the contamination of the recordings by environmental electric noise (see more details in Vandecasteele et al., 2012). After recovery, the probe was moved gradually in 70–150 μm steps per day until the desired position was reached. The operated animals were housed in individual cages. Neuronal recordings were performed daily for 20–30 days per animal to avoid the influence of gliosis as a reaction to possible damage caused by the electrodes over time. Recordings were performed by connecting the

probes to a signal multiplexing head-stage attached to a thin and light cable suspended from the room ceiling on a trolley system that allowed free movement of the animal. Recordings were made during running in a linear maze (50–60 trials) and sleeping sessions of 3–4 h. Water deprivation of the animals was maintained in periods of 6 days with 1-day rest of free water access. The spatial position of the rats during behavioral sessions was monitored using video tracking of two LEDs fixed to the head-stage. The wide-band signal was acquired at 20 kSamples/s (KJE-1001, Amplipex, Hungary), and processed off-line. The wide-band signal (0.2 Hz–10 kHz) was low-pass filtered and down sampled to 1250 Hz to generate LFP, and high-pass filtered (>500 Hz) for spike detection. The pyramidal layer in the CA1, 2 and 3 regions was identified physiologically by increased unit activity and the occurrence of LFP ripples (Ylinen et al., 1995, Mizuseki et al., 2011). The identification of dendritic sublayers in CA1, DG, and CA3 was achieved by the application of current source density (CSD) and independent component (ICA) analysis to the LFPs (Fernandez-Ruiz et al., 2012, 2013) and by known physiological markers such as the reversal of sharp-waves (Ylinen et al., 1995) and depth versus amplitude profile of theta oscillations (Buzsaki, 1986; Montgomery et al., 2009). The CA2 region was specifically identified post-hoc from histological sections by the thicker pyramidal layer and wider and sparser cell bodies compared to CA1 (Lorente de Nó, 1947, Chevaleyre and Siegelbaum, 2010) and confirmed by specific immunolabeling (anti-PCP4 antibody, Sigma HPA005792). CA3 area was divided into three approximately equally wide subregions as in (Lu et al., 2015): CA3a closest to the CA2 border (0% - 30% of the proximodistal axis), the intermediate part CA3b (between 30% and 60% of the axis) and CA3c within the dentate hilus (from 60 to 100% of the proximodistal axis) (Lorente de Nó, 1947). Segmentation was supported by the differences of cell density and thickness of the soma layer along the CA3 axis as reported previously (Lu et al., 2015). CA1 region was also split into three equally wide regions: CA1 proximal, closest to CA2, CA1 intermediate, in the middle, and CA1 distal, closest to subiculum.

Tissue Processing and Immunohistochemistry

After termination of the recordings, animals were deeply anesthetized and transcardially perfused with 0.9% saline solution followed by 4% paraformaldehyde solution. Brains were sectioned in 70-μm-thick slices (Leica Vibratome), with a 45° angle from the midline, parallel with the plane of the implanted electrodes. In addition, immunolabeling of the CA2 region with the specific marker PCP4, validated to label the cells in this region (Lein et al., 2005, Kohara et al., 2014), was performed. Slices were washed three times in PBS-Tx 1%, then blocked with 3% bovine serum albumin in PBS-Tx and incubated overnight at room temperature with the primary antibody solution containing rabbit anti-PCP4 (1:300, Sigma HPA005792). After three washes in PBS-Tx, sections were incubated for 2 h at room temperature with goat anti-rabbit Alexa Fluor488 (1:500, Jackson Immunoresearch 115-545-003) (Valero et al., 2015). Sections were then washed and mounted on glass slides with fluorescence medium (Fluoroshield with DAPI - F6057, Sigma, USA). Immunostained slices were examined and images were acquired with a confocal microscope (LSM880 Carl Zeiss) and/or with an epifluorescence microscope (AxioImager Carl Zeiss).

Data Analysis

Neuronal spikes were detected from the digitally high-pass filtered LFP (0.5 Hz–5 kHz) by a threshold crossing-based algorithm (Rossant et al., 2015). Detected spikes were automatically sorted using the masked EM algorithm for Gaussians mixtures implemented in KlustaKwik2 (Kadir et al., 2014), followed by manual adjustment of the clusters using KlustaViewa. Multiunit or noise clusters were discarded from further analysis. Cluster isolation quality was estimated by calculating the cluster characteristics (Csicsvari et al., 1998; Mizuseki et al., 2009; Stark et al., 2014), assisted by monosynaptic excitatory and inhibitory interactions between simultaneously recorded, well-isolated units (Bartho et al., 2004; Mizuseki et al., 2009).

Cross-correlation (CCG) analysis has been applied to indirectly detect putative monosynaptic connections (Csicsvari et al., 1998; Bartho et al., 2004; Fujisawa et al., 2008). CCG was calculated as the time resolved distribution of spike transmission probability between a reference spike train and a temporally shifting target spike train. A window interval of [−5, +5] ms with a 1 ms bin size was used for detecting sharp peaks or troughs, as identifiers of putative monosynaptic connections. Significantly correlated cell pairs were identified using the jittering method (Amarasingham et al., 2012). For each cell pair, surrogate data sets were constructed by randomly and independently jittering each spike's timestamp with a uniformly distributed value in the range of [−5, 5] ms, 1000 times. 99% acceptance bands were calculated from the surrogate data set CCGs for each bin, multiple comparison error was corrected by introducing "global significance bands" (Fujisawa et al., 2008). A cell pair was considered as having an excitatory monosynaptic connection, if any of its CCG bins reached above these global bands within the considered time window. The connection strength was quantified by calculating the standardized height of the monosynaptic peaks defined as:

$$\hat{h} = \frac{h - \mu_{\text{jitter}}}{\sigma_{\text{jitter}}}$$

where h is the peak height, μ_{jitter} is the jittered mean and σ_{jitter} is jittered standard deviation (Fujisawa et al., 2008).

Epochs of high theta (4–12 Hz) power during locomotion (with a minimum walking speed of 3 cm s^{-1}) were classified as RUN. Theta episodes during sleep were classified as REM. All states including slow-wave sleep (SWS) and quiet periods during wake state were detected using the ratio of the power in theta band (4–12 Hz) to delta band (1–4 Hz) of LFP, followed by manual adjustment with the aid of visual inspection of whitened power spectra and the raw traces (Sirota et al., 2008, Mizuseki et al., 2009, Mizuseki et al., 2011).

LFP of str. pyramidale was band-pass filtered (4–12 Hz) with a zero lag filter, yielding theta waves. Peaks of filtered waves were identified as the positive to negative zero crossings of the derivative (dy/dt), and phase was linearly interpolated between the peaks. Peaks are at 0° and 360° and troughs at 180° throughout the article. The mean resultant angle and length of the instantaneous theta phases of a given neuron's spikes were taken as the preferred phase and modulation strength of that neuron, respectively. For the preferred phase only neurons that were significantly modulated (Rayleigh test) by the theta oscillations were considered. Each cycle was divided into 36 bins for both measurements.

Positions of the linear track were projected onto the track axis. The position and spiking data were binned into 5-cm wide segments, generating the raw maps of spike number and occupancy probability. Rate map, number of place fields, spatial information (Skaggs et al., 1993), selectivity and sparsity (Skaggs et al., 1996) were calculated for each direction separately. A Gaussian kernel (SD = 5 cm) was applied to both raw maps of spike and occupancy, and a smoothed rate map was constructed by dividing the smoothed spike map by the smoothed occupancy map. A place field was defined as a continuous region, of at least 15 cm (THREE pixels), where the firing rate was above 10% of the peak rate in the maze, the peak firing rate was >2 Hz and the spatial coherence was >0.7. Place fields with fewer than 50 spikes and fields that included the turning position of the track were discarded. To compare the effect of subregions on the number of place fields one-way ANOVA was conducted, followed by post hoc student's *t* tests. The same method was used for comparisons between proximal, intermediate and distal CA1, as well as to compare the number of cells with one single place field across all subregions.

To visualize the theta phase advancement of spikes along the field traversal (phase-precession), the instantaneous theta phases (from the filtered CA1 pyramidal layer LFP) of spikes were plotted against the linearized positions in the track for each place field. Circular-linear regression between position and theta phase was applied to calculate the phase-precession slope and correlation strength (Kempter et al., 2012). This was performed by first fitting a linear regression model to circular-linear data by minimizing the circular error between measured and predicted angles. The slope of the resulting regression line was used to scale the linear variable (position) and to transform it into a circular one. Finally, a correlation coefficient analog to the Pearson's correlation was obtained. For further analyses, only fields displaying significant phase-position correlation ($P < 0.05$) were considered and their slope, correlation strength and phase range were calculated.

RESULTS

LFP and single units were recorded simultaneously from multiple CA regions of the hippocampus (CA1, CA2, and CA3; Fig. 1A,B) in eight rats. In all animals we recorded the CA1 region from the proximal (fimbrial) to the distal (subicular) poles, in six animals CA3 was sampled as well (CA3a, b and c) and in five animals the CA2 region was sampled, too. Recordings were carried out while rats run in a linear track for water reward or sleep in their home cages. The different regions were separated according to physiological criteria (Diba and Buzsaki, 2008; Mizuseki et al., 2009; Royer et al., 2010) and post-hoc immunohistological validation of electrode locations combined with PCP4 antibody staining (specific labeling for CA2 pyramidal cells). CA1 was divided into proximal, intermediate and distal parts and CA3 was separated into CA3c, CA3b, and CA3c. A total number of 1007 (CA1), 752 (CA3) and 512 (CA2) putative pyramidal cells and 171 (CA1), 125 (CA3), and 74 (CA2) putative interneurons were included in this study.

Spatial Coding Properties of CA1, CA2, and CA3 Place Cells

Place fields were identified during linear track running (Fig. 1C). A large fraction of CA1 (from all sites of the transverse axis) and CA2 cells were active place cells (at least one place field in either of both running directions) than CA3 neurons (grey bars in Fig. 1D; CA1 = 418 out of 607 cells, 68%; CA2 = 180 out of 273 cells, 66%; CA3 = 112 out of 214 cells, 42%; $P < 0.05$ for CA1/CA2 comparisons with CA3, rank sum test), in agreement with previous reports (Mizuseki et al., 2012; Lu et al., 2015). While within CA1 there was no significant difference ($F(2, 185) = 0.54$; $P = 0.6268$, one-way ANOVA), the number of active place cells progressively increased from CA3c to CA3a ($F(2, 45) = 3.6$; $P = 0.007$). This latter gradient appeared due to the gradual increase of the prevalence of multiple place field neurons, while the occurrence of the pyramidal cells with a single place field was not significantly different between the subregions (data not shown). In addition, the deep sublayer of CA1 (closer to stratum oriens) also displayed a larger number of place cells than the superficial sublayer ($P < 0.05$ for all CA1 subregions, rank sum test; Fig. 1D) (Mizuseki et al., 2011).

The number of place fields per cell also displayed regional differences. While place cells with more than one field were common in CA2, CA3a and distal CA1 (Fig. 1E; 32, 22, and 30% of cells with more than one field in CA2, CA3a and distal CA1 respectively; ANOVA test for mean number of fields versus regions, $F(6, 185) = 4.6$; $P = 0.041$), proximal CA1 and CA3c cells had preferentially one single place field (85 and 95% of cells with only one field in proximal CA1 and CA3c respectively; $F(6, 106) = 8.1$; $P = 0.040$). This result is in agreement with a previous study reporting larger number of place fields in distal compared to proximal CA1 cells in 2D environments (Henriksen et al., 2010), which was also the case in our data ($F(2, 185) = 5.1$; $P = 0.02$).

CA2 cells contained larger place fields while the sharpest where found in CA3c cells (Fig. 1F; $P < 0.01$ CA2 versus CA1 and CA3, rank sum test). Larger place fields were also found

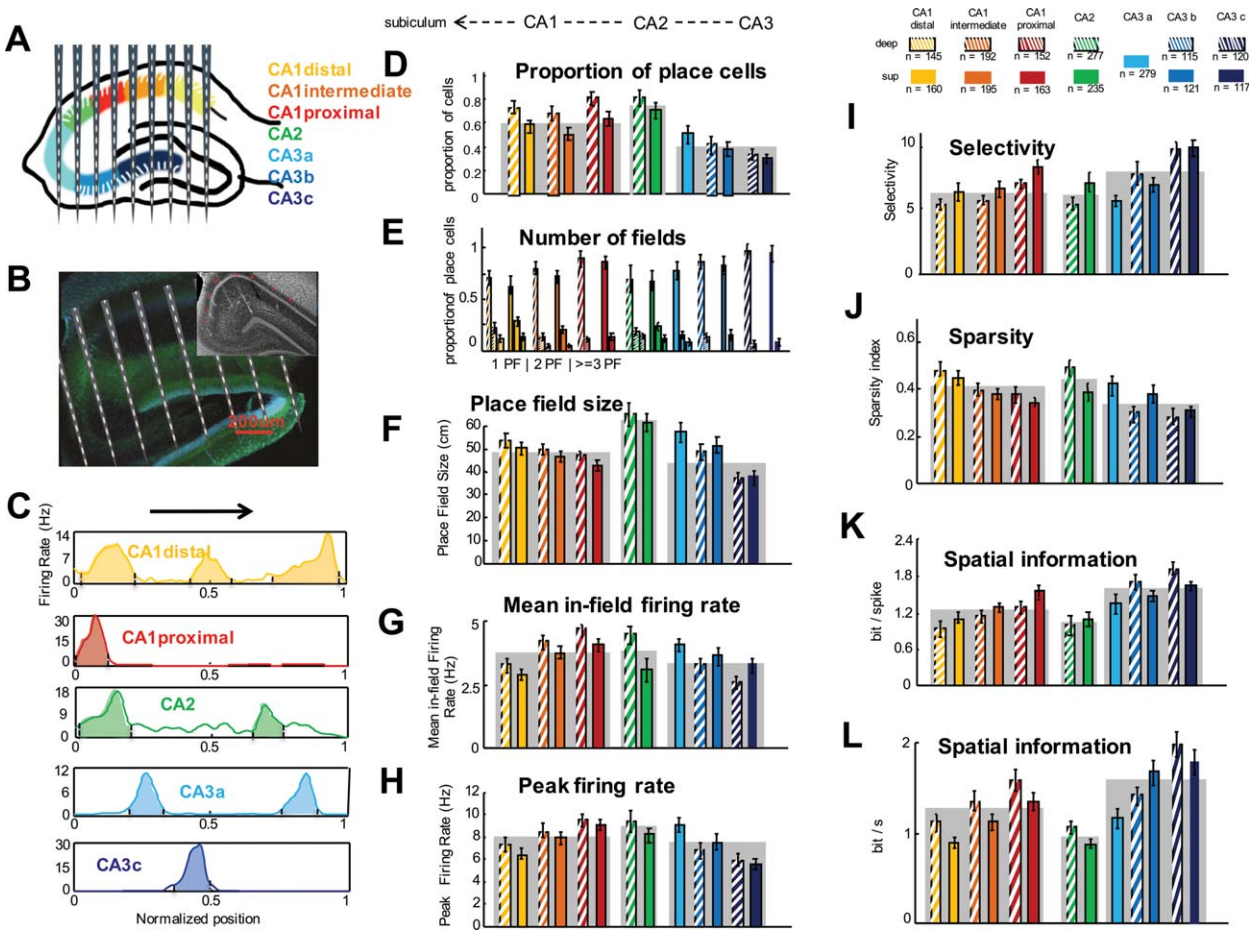

FIGURE 1. Spatial coding properties of place cells from different regions. A. Anatomical scheme of the recording sites. Different colors show different anatomical regions recorded (yellow: distal CA1, orange: intermediate CA1, red: proximal CA1, green: CA2, light blue: CA3a, medium blue: CA3b, dark blue: CA3c). Striped and solid parts of all regions show deep and superficial sublayers, respectively. B. Histological verification of the electrode locations and subregional boundaries within the hippocampus. PCP4 specific marker (green) is labeling the CA2pyramidal cells, while all somata are stained with DAPI (blue). Inset shows a section from the same animal with visible recording tracks crossing all subregions. C. Representative examples of place cells. Abscissae denote the normalized spatial location of the animal on the linear track. Proportion of place cells (D), number of place fields (E), place field size (F), mean in-field firing rate (G), peak firing rate (H), spatial selectivity (I), sparsity (J) and spatial information in bits per spike (K) as well as in bits per second (L) for all different subregions are plotted with their corresponding colors. Grey bars in the background represent averages of all subpopulations in a given region. [Color figure can be viewed at wileyonlinelibrary.com]

in distal CA1 cells compared to proximal ones while they were larger in CA3a and smaller in CA3c ($F(2, 247) = 3.6$; $P = 0.01$ and $F(2, 119) = 6.89$; $P = 0.0014$, ANOVA test for CA1 and CA3, respectively). No significant differences were found in deep compared with superficial cells (Fig. 1F; $P > 0.05$, rank sum test).

Deep cells in CA1 and CA2 showed higher firing rates inside their fields than superficial ones while in CA3 superficial cells were found to fire more than deep ones (Fig. 1G; $P < 0.05/0.05/0.01/0.001/0.01/0.01$ and 0.01 in distal CA1, intermediate CA1, proximal CA1, CA2, CA3a, CA3b, and CA3c respectively, rank sum test). The in-field mean firing rates were not significantly different from CA3 cells compared to CA1 and CA2, taken the regions as a whole, but were found to be different inside CA1 subregions (higher in proximal site, $F(2, 247) = 5.3$; $P = 0.039$) and inside CA3 subregions (higher in CA3a part, $F(2, 119) = 6.7$; $P = 0.0017$). Accordingly, the peak firing rates showed similar tendency, lower in CA3c than in CA3a ($F(2, 119) = 6.72$; $P = 0.0017$) and lower in CA1 distal than in proximal ($F(2, 247) = 4.6$; $P = 0.049$). Of all pyramidal cells, CA2 place cells had the highest peak firing rates ($P < 0.05$ for both comparisons, CA2-CA1 and CA2-CA3, rank sum test).

The reported differences in number and size of fields and firing rates matched the spatial information and specificity of place cells in the different regions. More selective place cells (calculated as peak in-field firing rate divided by mean firing rate in the track) were found in CA3 compared to CA1 and CA2 (Fig. 1I; $P < 0.01$ in both cases, rank sum test). Spatial selectivity increased gradually from distal to proximal CA1 and

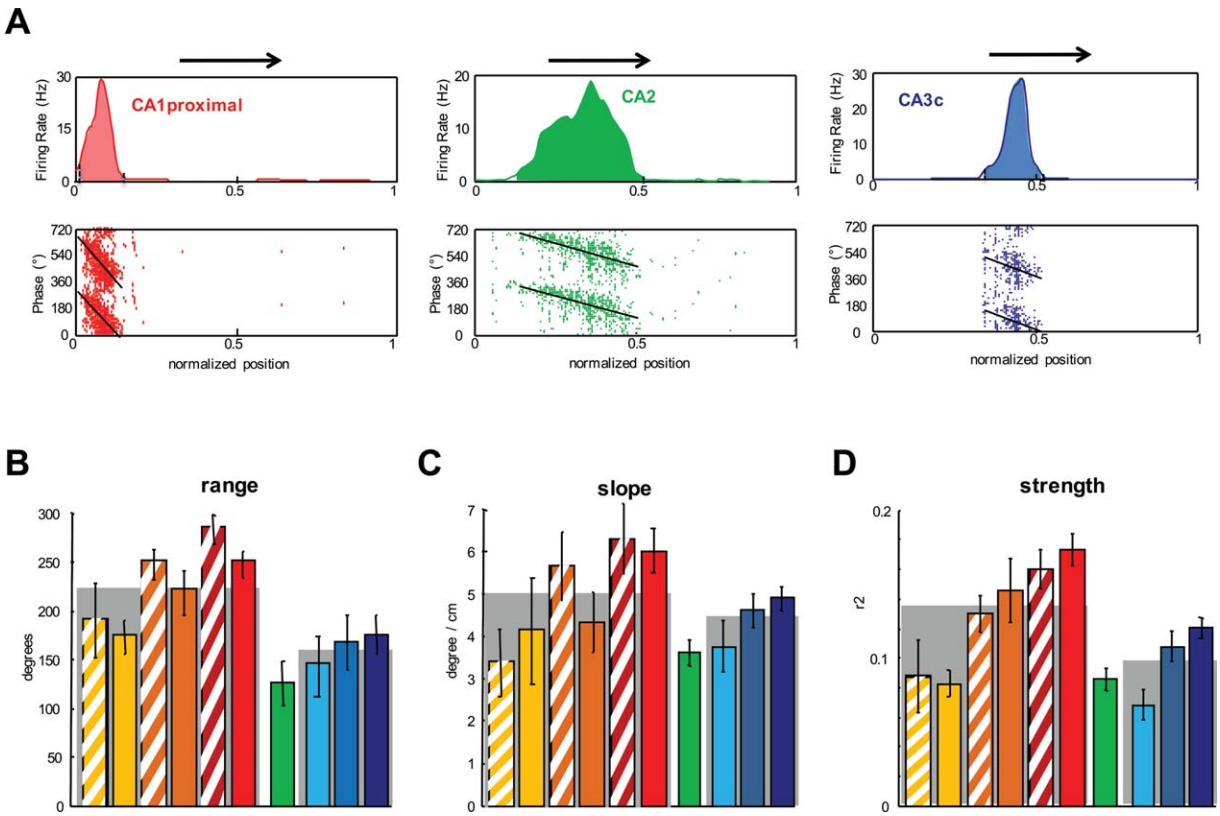

FIGURE 2. Phase Precession. A. Examples of phase-precessing place cells from different regions. Upper panels show firing rate maps and lower panels theta phase-position correlation of the spikes. B. The range of phase-precession was markedly shorter in CA3 and CA2 compared to CA1. C. Phase precession slopes were similar for CA1 subregions and smaller for CA3 and CA2. D. Phase-position correlation strength was larger in CA1 proximal cells and lower in CA2 and CA3a. [Color figure can be viewed at wileyonlinelibrary.com]

from CA3a to CA3c ($F(2, 185) = 6.2$; $P = 0.03$ and $F(2, 45) = 7.9$; $P = 0.038$, ANOVA). In agreement with this result, the sparsity of spatial representations (i.e., how sharply do the firing rate increase in a small region of space, e.g., sparsity close to zero correlates with a greater amount of spatial information) decreased from distal to proximal CA1 and from CA2 to CA3c (Fig. 1J; $F(2, 185) = 3.14$; $P = 0.043$ and $F(3, 45) = 7.49$; $P < 0.0001$). In general, superficial cells were more selective than deep ones in CA1 and CA2 ($P < 0.05$ and $P < 0.001$ for CA1 proximal and CA2 respectively, rank sum test) and less sparse ($P < 0.05$ and $P < 0.001$ for CA1 proximal and CA2 respectively).

The information content of spikes (in bits per spike) was higher for CA3 cells than for CA1 and CA2 neurons ($P < 0.01$ for CA3 versus CA1 and $P < 0.001$ for CA3 versus CA2, rank sum test; Fig. 1K). Spatial information decrease from distal to proximal CA1 and from CA2 to CA3c ($F(2, 185) = 3.91$; $P = 0.021$ and $F(3, 180) = 3.87$; $P = 0.0098$). For the CA1 region, superficial cells carried more information per spike than the deep ones ($P < 0.05$ for all subregions, rank sum test), while for the CA3 region, deep cells were more informative ($P < 0.05$ for all subregions, rank sum test). The spatial information rate (bits per second) was also higher in CA3 and lower in CA1 and CA2 (Fig. 1L; $P < 0.05$ and $P < 0.01$ for comparison with CA1 and CA2, rank sum test) and also gradually increase form distal CA1 to proximal CA1 and from CA2 to CA3c ($F(2, 185) = 2.7$; $P = 0.042$, and $F(3, 180) = 4.26$; $P = 0.005$). However, in this case the CA1 and CA2 deep sublayer had a higher information rate than the superficial one ($P < 0.05$, rank sum test for all comparisons). This apparently contradictory result for the deep and superficial CA1 sublayers was previously reported and accounted for the higher firing rates of deep cells (Fig. 5) (Mizuseki et al., 2011).

In summary, place cells in CA3 region are more likely to have only one field and code more spatial information compared to CA1 and CA2 cells. Better spatial coding was found in CA3c cells compared to CA3a ones and also for proximal CA1 cells compared to their distal peers. CA2 cells were found to code poorly for space, in agreement with previous observations (Mankin et al., 2015).

Phase-precession in CA1, CA2, and CA3 Place Cells

During spatial navigation, hippocampal place cells also exhibit a temporal code manifested by a progressive theta phase

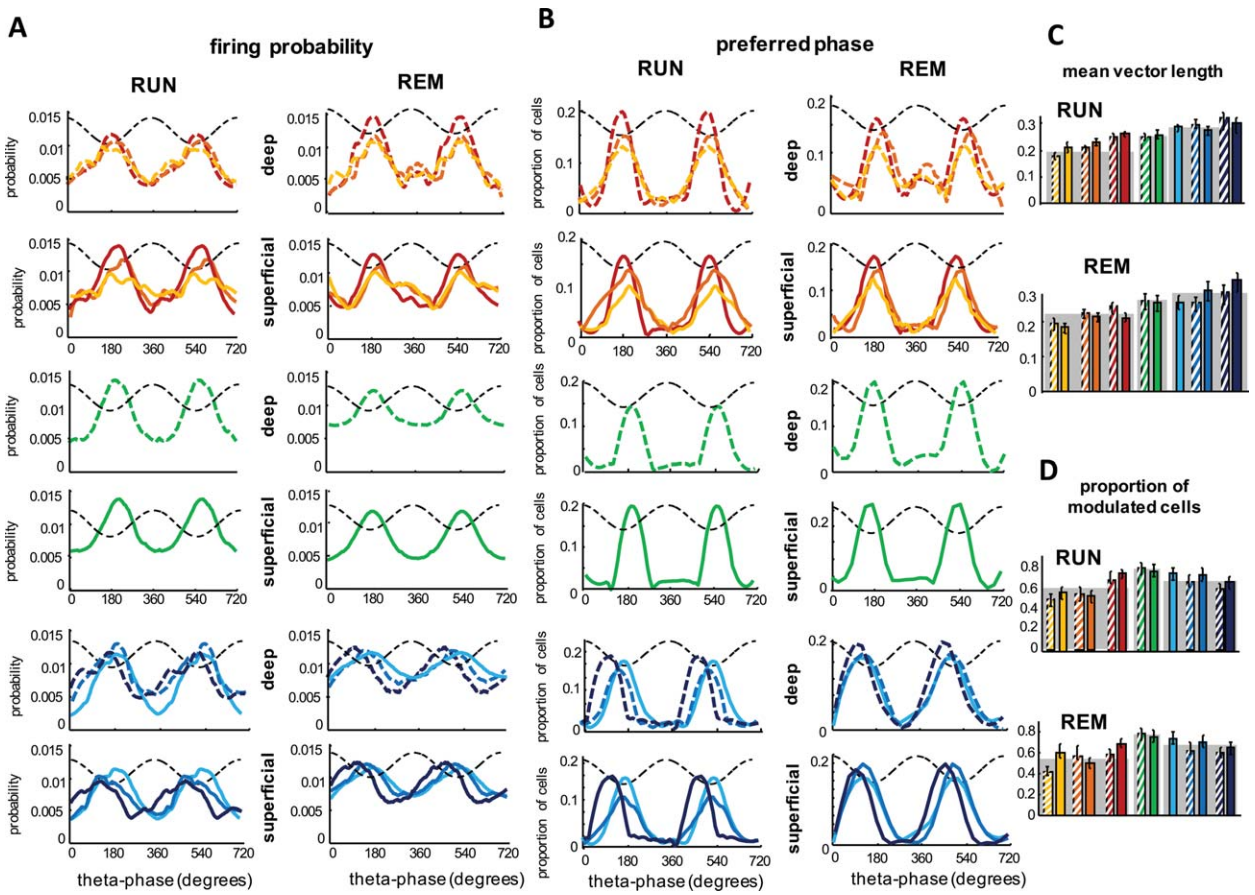

FIGURE 3. Theta phase modulation of hippocampal pyramidal cells. A. Population discharge probability of pyramidal cells from the different subregions as a function of CA1 pyramidal layer theta phase (dotted black line) during RUN and REM sleep. All pyramidal cells were included. Two theta cycles are shown for better clarity. B. Distribution of preferred theta phases for all significantly modulated units ($P < 0.01$, Rayleigh test) in all regions during RUN and REM. C. Modulation strength by theta oscillations (mean vector length). Note the gradient from proximal CA1 (stronger theta modulated) toward distal CA1 (less theta modulated) during RUN. [Color figure can be viewed at wileyonlinelibrary.com]

shift of the spikes as the animal traverses through the neuron's place field, also known as phase-precession (O'Keefe and Recce, 1993). Spikes occurring later in the field tend to appear at an earlier phase of the theta cycle. Only fields displaying a significant phase-position correlation ($P < 0.05$, circular-linear regression) were considered for this analysis. In all cases, the reference theta phase was taken from the middle of the CA1 pyramidal layer, the peak being 0° and 360° and the trough 180°. All CA1 subregions displayed a strong phase-precession with a mean phase-shift of 240 degrees inside the place field (Fig. 2; proximal CA1 = 105 fields, CA1 intermediate = 106 fields, CA1 distal = 88 fields). In comparison, phase-precession in both CA2 and CA3 was much reduced, spanning 127 and 161 degrees on average, respectively (Fig. 2B,C; CA2 = 75 fields, CA3a = 30, CA3b = 44, CA3c = 78). Accordingly, the distribution of phase ranges across place fields was larger for CA1 subregions and increased from distal to proximal sites (Fig. 2B; 186°/231°/266° mean for CA1 proximal/intermediate/distal; $F(2, 247) = 3.75$; $P = 0.024$) and significantly shorter for CA2 (127° mean; $P < 0.0001$ for all comparison with CA1, rank sum test) and CA3 (147°/160°/171° mean; $P < 0.001$ for all comparisons with CA1, rank sum test). CA1 cells in the deep sublayers had a tendency to span a larger range of phases than their superficial peers (Fig. 2B).

The differences of phase precession properties across regions were also illustrated by the distributions of regression slopes and the strength of phase-position correlation. Slopes were steeper for all CA1 subregions than CA2 or CA3 (Fig. 2C; $P < 0.01$ for CA2–CA1 comparison and $P < 0.05$ for CA3–CA1, rank sum test) as well as phase-position correlation strength (Fig. 2D; $P < 0.01$ for comparisons of CA3 and CA2 with CA1, rank sum test). Correlation strength also increased from distal to proximal CA1 ($F(2, 247) = 4.46$; $P = 0.012$) and CA3a to CA3c ($F(2, 247) = 2.63$; $P = 0.043$).

Modulation of Neurons by Theta Oscillations

Neurons in the hippocampus are strongly theta modulated during exploration and REM sleep (Buzsaki et al., 1983). We thus asked whether the reported differences in spatial and

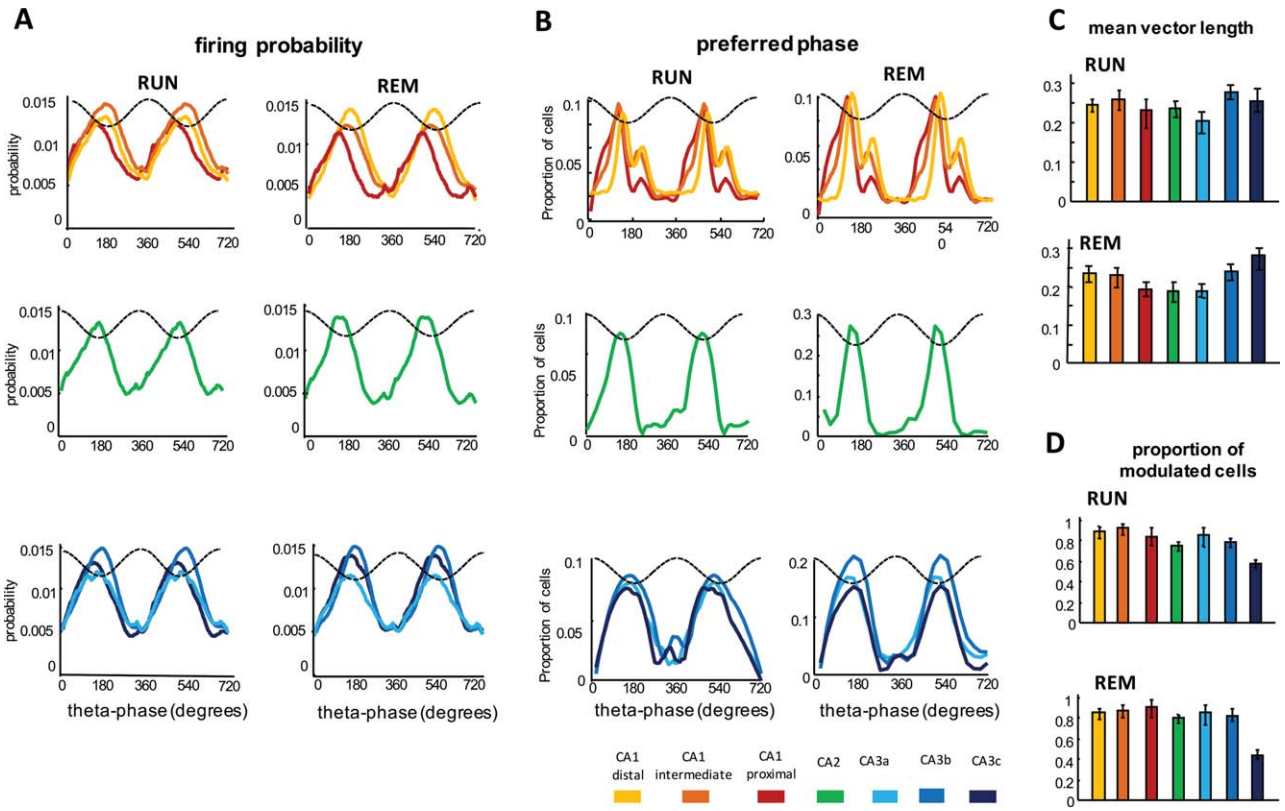

FIGURE 4. Theta phase modulation of hippocampal interneurons. A. Population discharge probability of interneurons from the different subregions as a function of CA1 pyramidal layer theta phase (dotted black line) during RUN and REM sleep. All interneurons were included. Two theta cycles are shown for better visualization. B. Distribution of preferred theta phases for all significantly modulated units ($P < 0.01$, Rayleigh test) in all regions during RUN and REM. C. Modulation strength by theta oscillations (mean vector length). [Color figure can be viewed at wileyonlinelibrary.com]

temporal coding of hippocampal cells across regions corresponded with differences in spike-theta phase relationship. For this purpose, we used two complementary measures: the theta phase distribution of spikes from a given population (Figs. 3A and 4A) and the distribution of preferred firing phase of single units (Fig. 3B). We analyzed separately pyramidal cells (Fig. 3) and interneurons (Fig. 4). Local theta phases were used for these analyses taken from the middle of the CA1 pyramidal layer of each shank.

In general, CA3 pyramidal neurons were more strongly phase-locked to theta oscillations than CA2 and CA1 cells during RUN and REM (Fig. 3A,C; $P < 0.01$ and $P < 0.05$ for comparisons with CA2 and CA1, rank sum test). Theta modulation strength increased form distal CA1 to proximal CA1 and from CA3a to CA3c during RUN ($F(2, 236) = 14.34$; $P < 0.001$ and $F(2, 217) = 3.1$; $P = 0.02$ for RUN) while during REM state a gradient was notable from CA3a toward CA3c ($F(2, 217) = 3.3$; $P = 0.047$). In addition, differences were noted between deep and superficial CA1 during different states. While during RUN superficial CA1 cells had higher theta modulation strength than deeper ones ($P < 0.05$ for distal CA1, rank sum test), during REM state the deeper cells were stronger theta modulated ($P < 0.01$ for proximal CA1). In all regions, theta modulation strength was higher during REM compared to RUN state ($P < 0.05$ for all comparisons, rank sum test).

The proportion of significantly theta modulated cells ($P < 0.01$, Rayleigh test) was also higher in proximal CA1 compare to distal CA1 and in CA2 compare to all CA3 regions ($F(2, 236) = 3.31$; $P = 0.042$, $F(3, 407) = 3.1$; $P = 0.039$).

It has been previously reported that neurons in different regions fire preferentially at distinct phases of the theta cycle during both, RUN and REM states (Mizuseki et al., 2012; Schomburg et al., 2014). In line with previous reports, CA3 neurons fired, on average, at earlier theta phases than CA1 (Mizuseki et al., 2012) or CA2 neurons (Fig. 3B). While the preferred theta phase for neurons at all CA1 subregions was similar (182°/186°/184° medians preferred phases, $p > 0.05$, ANOVA), CA3c fired, on average, earlier (at the descending theta phase) than CA3a or CA3b (100°/180°/170° medians preferred phases, $F(2, 217) = 34.1$; $P = 0.015$). CA2 cells showed a very sharp distribution firing at a similar phase to CA1 and CA3a cells, the early ascending theta phase.

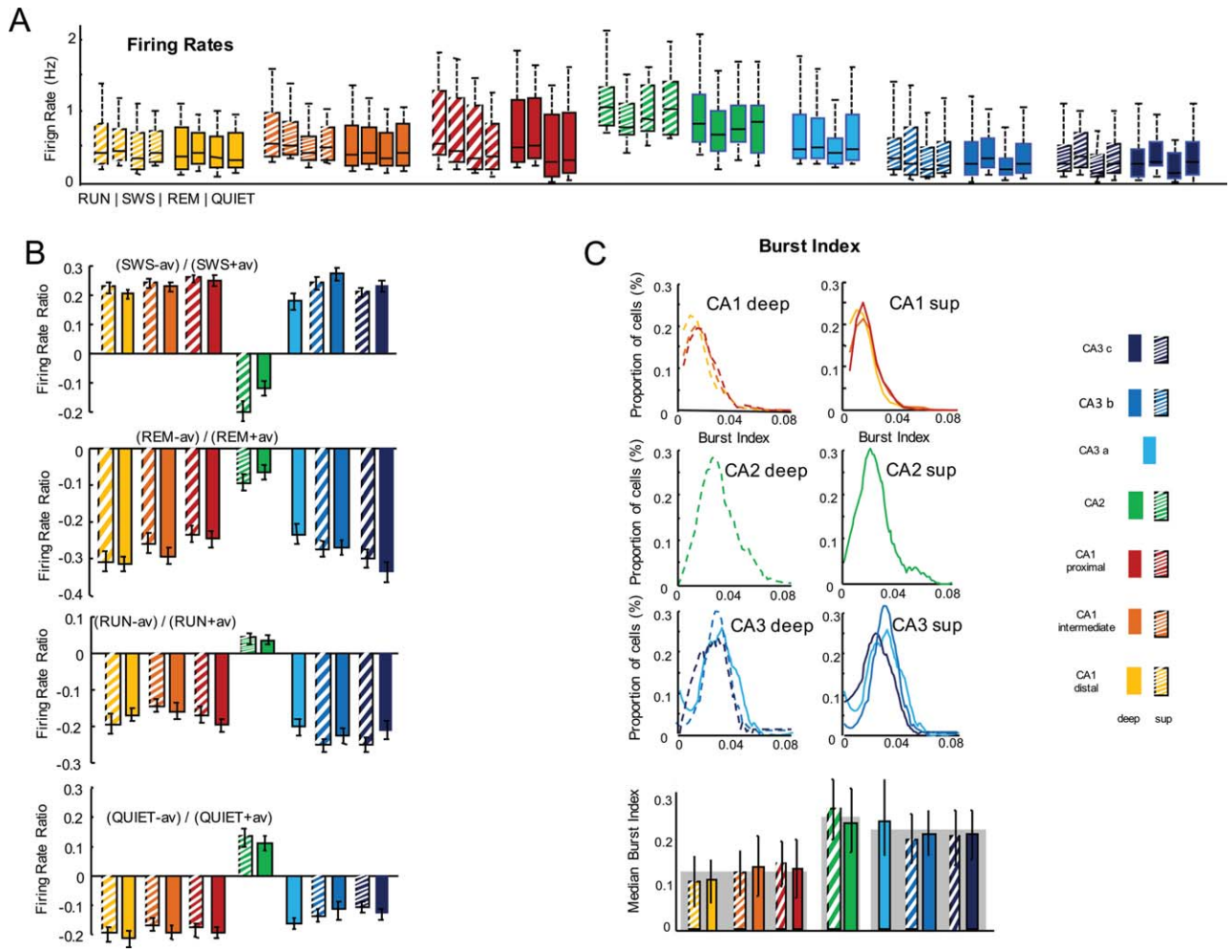

FIGURE 5. Brain state-dependent firing rates of CA1, CA2, and CA3 principal cells. A. Firing rate distributions during RUN, SWS, REM, and QUIET states. B. Firing rate modulation during various behavioral states compared to an idealized average firing rate (av: non-weighted mean of the firing rates during the four discriminated states). C. Burst index distribution for deep and superficial neurons of all subregions. Medians with deviations are showed below. [Color figure can be viewed at wileyonlinelibrary.com]

A strong difference appeared when comparing the preferred phase distribution (and to a less extent also the firing probability distributions) of CA1 cells during RUN and REM. A large proportion of deep cells shifted their preferred phase from closer to the trough to the theta peak (Fig. 3B right panel in first row). This "REM shifting" behavior (Mizuseki et al., 2011) was absent in both CA2 and CA3 cells.

Interneurons were, in general, more strongly theta modulated than pyramidal cells in all regions (Fig. 4A–C) as well as they had a higher proportion of significantly modulated cells (Fig. 4D). Contrary to the region-dependent phase preference of pyramidal cells (Fig. 3B), the firing probability of CA1, CA2, and CA3 interneurons was maximal closer to the theta through and smallest at the peak (Fig. 4A). However, the distribution of preferred phases revealed that a significant proportion of CA1 and, to lower extent, CA3 interneurons tended to fire during the ascending theta phase during both RUN and REM states. Inside CA1, the proportion of interneurons firing at the ascending theta phase showed no dependency on subregions. In addition, the strength of theta modulation decreased from distal to proximal CA1 and from CA3c to CA3a (Fig. 4C; $F(2, 236) = 2.28$; $P = 0.044$ and $F(2, 217) = 4.1$; $P = 0.037$ for CA1 and CA3, respectively during RUN; $F(2, 236) = 3.31$; $P = 0.045$ and $F(2, 217) = 5.2$; $P = 0.025$ for CA1 and CA3, respectively, during REM) although the proportion of significantly theta modulated interneurons was lower in CA3c (Fig. 4D).

Firing Patterns of Different Regions in Distinct Brain States

Next, we asked whether firing patterns of single pyramidal cells in the different regions were dependent on brain states.

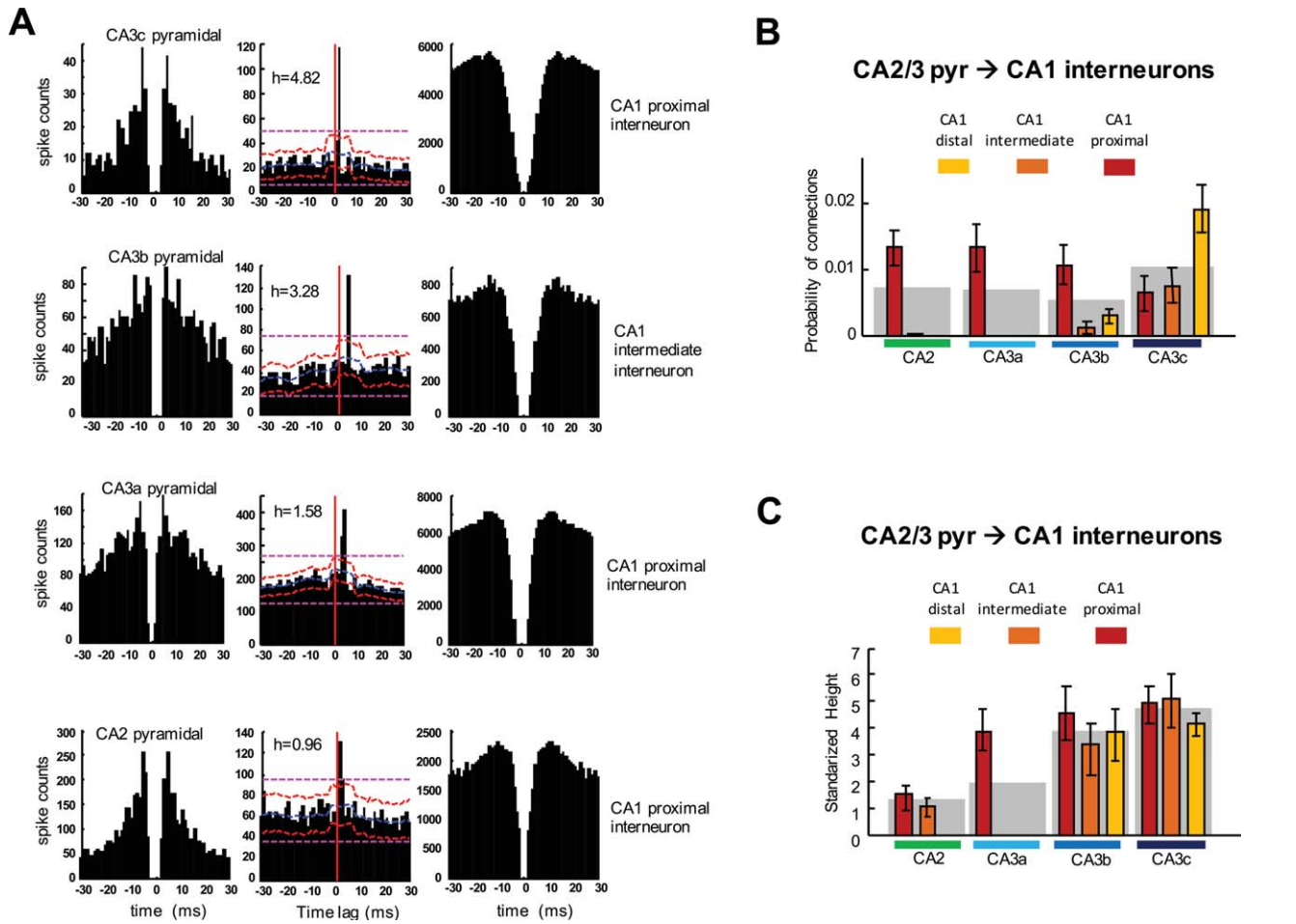

FIGURE 6. Functional connectivity inside the hippocampal transverse axis. Putative monosynaptic connections from different regions to distinct sites of CA1 (proximal, intermediate, distal). A. Examples of different putative monosynaptic pairs between different regions. For each example the autocorrelograms (left and right panels) and the crosscorrelogram of the given pair (middle panel) is shown. Red and magenta lines denote the local and global confidence levels for significance test, respectively. "h" value of the crosscorrelogram shows the standardized height of the monosynaptic peaks. B. Probability of monosynaptic connections. Amongst CA2 and CA3 regions, CA3c is the most likely to project to CA1. Proximal CA1 gets more inputs from all other subregions than other CA1 subregions. C. Mean strength of monosynaptically connected pairs. Notice the different strength of connectivity between CA3-CA1 (all sites) and CA2-CA1. [Color figure can be viewed at wileyonlinelibrary.com]

The overall firing rates of CA2 cells were the highest for all brain states, followed by CA1, which were also higher with respect to CA3 (Fig. 5A, $P < 0.001$ for CA2–CA1 and $P < 0.01$ for CA3–CA1 comparisons, rank sum test). In CA1 and CA2, deep layer cells had also higher firing rates for all states than their superficial peers ($P < 0.01$ for CA1 and CA2, signed rank test). There was a gradient of increasing firing rates from the distal to the proximal poles of CA1 ($F(2, 387) = 15.25$; $P < 0.001$) and from CA3c toward CA3a ($F(2, 279) = 6.76$; $P = 0.0012$).

The highest mean firing rates were found during RUN state for all regions except CA2 ($F(3, 1007) = 20.42$; $P < 0.001$). CA2 had higher firing rate during QUIET than during any other state ($F(3, 1007) = 4$; $P = 0.007$, see also Fig. 5B), and this difference was more pronounced for deep than superficial cells ($P < 0.01$, rank sum test). During REM sleep, firing rates were generally lower, especially for CA1 superficial sublayer ($P < 0.05$ for all subregions, rank sum test) and CA3c ($F(2, 279) = 3.04$; $P = 0.046$, see also Fig. 5B).

To assess the temporal firing dynamics of single neurons, we defined a burst index as the proportion of spikes with <6 ms inter-spike intervals burst versus the total number of spikes (Harris et al., 2001). The distribution of burst index showed a markedly higher probability for burst spiking for CA3 and CA2 cells compared to CA1 cells (Fig. 5C, $P < 0.01$ for CA3-CA1 and $P < 0.001$ for CA2-CA1 comparisons, rank sum test), and within CA1 and CA2 bursting was higher for deep than superficial cells ($P < 0.05$ and $P < 0.01$ for CA1 and CA2, respectively, rank sum test). Along the CA3 axis, burst tendency decreased from CA3a to CA3c ($F(2, 279) = 3.37$; $P = 0.034$).

Function Connectivity between Regions

Our large-scale recordings also allowed to study monosynaptic connections between neurons of different regions (Fujisawa et al., 2008). We examined cross-correlograms of pyramidal cell-interneuron pairs and calculated the spike transmission probability within monosynaptic time window (<5 ms) to identify putative synaptic connections between cells from the different regions (Fig. 6A).

We found functional connections to CA1 interneurons from all subfields of CA3 and CA2. CA2 and CA3a projected with higher probability to proximal CA1 (Fig. 6B, $P < 0.01$ for all comparisons, rank sum test) while CA3c projected preferentially to distal CA1 ($F(2, 387) = 5.5$; $P = 0.049$). Among the CA3 subregions, CA3c was the most probable to drive interneurons in each of the CA1 subregions ($F(2, 279) = 5.33$; $P = 0.033$). Interestingly, the strength of the connectivity between the different regions was very different. CA3-CA1 pyramidal-interneurons pairs had higher spike transmission probability than CA2-CA1 pairs. Within CA3, the strength slightly increased from CA3a to CA3c (Fig. 6C,$F(2, 279) = 3.21$; $P = 0.044$).

DISCUSSION

Hippocampal pyramidal neurons in the CA1, CA2, and CA3 regions showed distinct spatial coding properties, theta rhythm modulation, behavioral state-dependent firing rates, and burst patterns. Physiological differences also emerged when neurons were compared at different locations along the transverse or dorsoventral axis with these main regions, suggesting a tight coupling between physiology, changing connectivity and cellular/molecular properties along hippocampal subregions and across sublayers.

The fraction of CA3 place cells was lower than those in CA1 and CA2 regions but their coding was more selective and informative, due mainly to the fewer place fields per neuron in the CA3 region. Less specific spatial coding was observed in the CA2 region and the distal segment of CA1. The range and strength of phase precession was markedly higher for CA1 place cells than for CA2 and CA3 pyramidal neurons.

CA3 pyramidal cells had stronger theta modulation than CA1 cells and fired earlier in the theta cycle on average. CA2 neurons fired at a similar theta phase as CA1 neurons but were more strongly theta-modulated, commensurate with their more limited phase-precession. CA1 but not CA2 and CA3 pyramidal cells shifted their preferred firing phase towards the theta peak during REM sleep.

Spatial Coding Properties of CA1, CA2, and CA3 Place Cells

All principal cells in the hippocampus are selectively responsive to environmental and local cues during spatial navigation (O'Keefe and Dostrovsky, 1971). Yet, differences in their coding properties have already been noted in different hippocampal regions (Skaggs et al., 1996, Leutgeb et al., 2004). While fewer principal cells displayed space-dependent responses in CA3 (53%) than in CA1 (72%), CA3 place cells were more selective, and their spikes more spatially informative (Fig. 1), consistent with previous reports (Leutgeb et al., 2004, Mizuseki et al., 2012). Place cells in the proximal segment of CA1 were more spatially informative than the distal CA1 segment, as was also observed in two-dimensional environments (Henriksen et al., 2010). These results had been attributed to the different inputs reaching the CA1 region. Axons from MEC, where the highly spatially selective grid cells are located (Hafting et al., 2005), preferentially target the proximal CA1, while axons from LEC, where less spatially modulated cells are found (Knierim and Neunuebel, 2016), terminate on the distal part (Tamamaki et al., 1988, Witter et al., 2000, Naber et al., 2001). Furthermore, the dominance of theta-modulated CA3 inputs to proximal CA1 (Schomburg et al., 2014) could contribute to the highly selective place cells of proximal CA1 subregion.

Remarkable differences were noted between place cells located in deep and superficial sublayers of CA1. Larger fraction of deeply located pyramidal neurons was spatially modulated, consistent with previous work (Mizuseki et al., 2011), and this difference was present along the entire proximo-distal axis. Although a number of anatomical and molecular observations can contribute to the functional stratification of CA1 pyramidal layer (Thompson et al., 2008, Dong et al., 2009), their differential afferents likely play a critical role. Deep CA1 neurons are preferentially driven by medial entorhinal input layer 3 neurons (Mizuseki et al., 2011) with higher spatial selectivity than those in the lateral entorhinal cortex (Hargreaves et al., 2005). These combined differences in both the proximo-distal and dorsoventral directions suggest that the dorsoventral divisions are of unequal proportions in the different CA1 subregions so that the fraction of "deep type" neurons with strong spatial features increases gradually from the distal to proximal direction.

For CA3 neurons, a gradient in spatial selectivity was observed from CA3c (highly selective and informative) toward CA3a, consistent with recent observations (Lee et al., 2015, Lu et al., 2015). Again, this finding is in line with the gradient of changing connectivity in this region. The numbers of mossy fiber inputs decrease from CA3c toward CA3a, while the recurrent, associational (recurrent) projections between pyramidal cells, as well as the number of axons from layer II of entorhinal cortex become more prominent (Ishizuka et al., 1990; Li et al., 1994; Ishizuka et al., 1995). We also found that while the fractions of place cells were similar across CA3 subregions, the prevalence of neurons with multiple place fields gradually increased toward CA3a.

The CA2 region has been under intense investigation recently (Hitti and Siegelbaum, 2014; Mankin et al., 2015; Dudek et al., 2016; Kay et al., 2016). The fraction of place cells was greater in this subregion compared to CA1, but place field

selectivity was less, indicating relatively poor spatial coding by these neurons during explorative behavior. On the other hand, a special coding for space during immobility was recently suggested as a possible complementary role of CA2 (Kay et al., 2016).

Our functional connectivity analysis (Fig. 6) matched and complemented the anatomical data showing that CA3c area innervates strongly interneurons in the distal CA1 segment and gradually less so in the more proximal segments. In contrast, CA3a and CA2 axons preferentially target proximal CA1 interneurons (Tamamaki et al., 1988; Ishizuka et al., 1990). According to this wiring scheme, CA1 proximal sites receive a stronger combination of place cell inputs from the spatially modulated MEC inputs and CA3. Distal CA1 neurons, on the other hand, receive CA3c inputs, where the proportion of place cells is lower, together with low spatially selective LEC innervations. The combination of these inputs may account for the sparser and less accurate spatial coding of distal CA1 cells.

Phase Precession in CA1, CA2, and CA3 Regions

At the entrance of their place field, place cells tend to fire close to the theta peak and this phase preference shifts toward earlier phases in the theta cycle as the animal traverses the place field (O'Keefe and Dostrovsky, 1971; Huxter et al., 2003). In the CA1 region, the range of phase precession was wide, spanning more than 200°, thus at the last part of the field, place cells fired at the descending theta phase. In contrast, the range of phase precession in CA2 and CA3 regions was strikingly smaller, spanning only 130–170°. In addition, the slope and strength of the phase-position correlation of spikes with place fields was higher for CA1 than for CA2 or CA3 place cells. Other studies have also shown that CA3 and putative dentate gyrus place cells have a shorter range of phase-precession than those in CA1 (Skaggs et al., 1996; Mizuseki et al., 2012).

Finally, the strength of the spike phase-position correlation was significantly higher for proximally located CA1 cells. This difference may reflect the more spatially tuned and stronger theta modulated MEC input reaching proximal CA1 compared to the distal segment, which is mainly under the control of LEC (Witter et al., 2000; Naber et al., 2001; Hargreaves et al., 2005).

Theta Phase Locking of CA1, CA2, and CA3 Cells and Behavioral Correlates

Although an extensive literature demonstrates theta phase-locking of hippocampal neuronal spiking (Csicsvari et al., 1999; Buzsaki, 2002), the present study offers a comprehensive quantification of the theta dynamics of cells across all hippocampal subregions. On average, CA3 cells were significantly more strongly theta phase-locked than CA1 and CA2 pyramidal cells during both running and REM sleep. The preferred theta phase of principal cells gradually shifted from the early ascending phase in CA1 to the descending phase in CA3c (Fig. 3).

Quantitatively different phase preferences were also noted between deep and superficial neurons of the CA1 but not other regions in distinct behavioral states. While the majority of superficial CA1 neurons showed similar firing phase preference during REM and RUN, a subset of deep cells shifted 180° during REM state (Mizuseki et al., 2011). This phase shift is likely due to the stronger entorhinal layer III inputs during REM sleep arriving at the peak of CA1 pyramidal layer theta (Mizuseki et al., 2009; Schomburg et al., 2014). Entorhinal layer III only projects to CA1, and this projection is stronger to CA1 deep cells, while CA2 and CA3 neurons only receive entorhinal layer II inputs (Witter et al., 2000; Kohara et al., 2014), which are fire mainly at the theta trough (Mizuseki et al., 2009).

CA3a displayed a theta phase preference similar to CA1 and CA2, whereas a shift to the descending phase appeared toward the CA3c subregion. The different behavioral states had no influence on the theta phase preference of the CA3 cells, but a stronger phase locking was present in REM state than during running. CA3c is strongly innervated by mossy fibers but receives less entorhinal inputs than CA3a (Ishizuka et al., 1990; Li et al., 1994; Ishizuka et al., 1995), which difference may contribute to the lower percentage of theta-modulated cells in CA3c than CA3a.

The theta phase preference of interneurons was similar across the different regions (Fig. 4). The majority fired at the descending phase or theta trough but a minority preferred the ascending phase or even the theta peak, mainly in CA1. These different theta-phase preferences of interneurons presumably correspond to subsets of the many types of hippocampal interneurons that have been reported to have different phase-locking to theta and other oscillations (Klausberger and Somogyi, 2008).

Pathophysiological Consequences of the Nonuniform Physiological Properties along the Cornu Ammonis Subregions

The behavioral state of the animal had a notable effect on the firing rates in the distinct regions and subregions. In general, all neurons fired more intensely during RUN state than in any other state, with the notable exception of higher firing rates of CA2 pyramidal neurons during quiet wakefulness (Fig. 5). During REM sleep CA3 neurons, and in particular CA3c, decreased their firing rates (Montgomery et al., 2009), resulting in a decreased CA3 to CA1 oscillatory input during REM (Fernandez-Ruiz et al., 2012; Schomburg et al., 2014). In all brain states, the proximal superficial segment of CA1 was more active than the CA1 in the remaining subregions and in CA2.

The CA2 region was the most excitable followed by CA3a region, as reflected by higher burst tendency and overall firing rates. The higher firing rates and bursting properties of CA2 neurons in combination with their strong recurrent collaterals (Tamamaki et al., 1988) make CA2 neurons prone to synchrony. This is in agreement with our recent demonstration that the CA2 regions is the typical initiator of hippocampal sharp

wave-ripples, particularly in the waking animal (Oliva et al., 2016). This high excitability of the CA2 population also makes it a vulnerable region in disorders. In vitro studies using GABAA receptor antagonists also showed that epileptic spikes originate in CA2, and computational studies corroborate the CA2 region as a substrate of neuronal synchronization during epilepsy (Traub and Wong, 1982; Wong et al., 1986). Data from human studies further support the key role of CA2 in the initiation of hypersynchronous pathological events (Avoli et al., 2016).

Overall, our findings show substantial heterogeneity among hippocampal subregions. Spatial coding properties are quantitatively different among the main regions (CA1, CA2, and CA3) but also vary within regions (from proximal to distal CA1 and from CA3c toward CA3a and CA2). These differences were robust in terms of both single cell properties and circuit organization. Quantitatively different behavioral correlates exist even across subregions, including the less investigated CA2 region. Further experiments, including simultaneous recordings from the dentate gyrus, medial and lateral entorhinal cortex are needed to provide a complete functional map of the circuit dynamics and cellular interactions within the hippocampal formation.

Acknowledgments

The authors thank Daniel English and Brendon Watson for insightful comments; Péter Hegyi for providing access to confocal microscopy; Gergő Nagy for experimental assistance. A.B. is the founder of Amplipex Ltd., which manufactures signal-multiplexed headstages and demultiplexing systems.

REFERENCES

Amaral L. 2007. Hippocampal neuroanatomy. In: Andersen P, et al., editor. The Hippocampus Book. New York, NY: Oxford University Press. pp 37–114.

Amaral DG, Witter MP. 1989. The three-dimensional organization of the hippocampal formation: A review of anatomical data. Neuroscience 31:571–591.

Amarasingham A, Harrison MT, Hatsopoulos NG, Geman S. 2012. Conditional modeling and the jitter method of spike resampling. J Neurophysiol 107:517–531.

Avoli M, de Curtis M, Gnatkovsky V, Gotman J, Kohling R, Levesque M, Manseau F, Shiri Z, Williams S. 2016. Specific imbalance of excitatory/inhibitory signaling establishes seizure onset pattern in temporal lobe epilepsy. J Neurophysiol 115:3229–3237.

Bannister NJ, Larkman AU. 1995. Dendritic morphology of CA1 pyramidal neurones from the rat hippocampus: II. Spine distributions. J Comp Neurol 360:161–171.

Bartho P, Hirase H, Monconduit L, Zugaro M, Harris KD, Buzsaki G. 2004. Characterization of neocortical principal cells and interneurons by network interactions and extracellular features. J Neurophysiol 92:600–608.

Berenyi A, Somogyvari Z, Nagy AJ, Roux L, Long JD, Fujisawa S, Stark E, Leonardo A, Harris TD, Buzsaki G. 2014. Large-scale, high-density (up to 512 channels) recording of local circuits in behaving animals. J Neurophysiol 111:1132–1149.

Bittner KC, Grienberger C, Vaidya SP, Milstein AD, Macklin JJ, Suh J, Tonegawa S, Magee JC. 2015. Conjunctive input processing drives feature selectivity in hippocampal CA1 neurons. Nat Neurosci 18:1133–1142.

Burke SN, Maurer AP, Nematollahi S, Uprety AR, Wallace JL, Barnes CA. 2011. The influence of objects on place field expression and size in distal hippocampal CA1. Hippocampus 21:783–801.

Buzsaki G. 1986. Hippocampal sharp waves: Their origin and significance. Brain Res 398:242–252.

Buzsaki G. 2002. Theta oscillations in the hippocampus. Neuron 33: 325–340.

Buzsaki G, Leung LW, Vanderwolf CH. 1983. Cellular bases of hippocampal EEG in the behaving rat. Brain Res 287:139–171.

Carstens KE, Phillips ML, Pozzo-Miller L, Weinberg RJ, Dudek SM. 2016. Perineuronal nets suppress plasticity of excitatory synapses on CA2 pyramidal neurons. J Neurosci Off J Soc Neurosci 36: 6312–6320.

Cembrowski MS, Wang L, Sugino K, Shields BC, Spruston N. 2016. Hipposeq: A comprehensive RNA-seq database of gene expression in hippocampal principal neurons. eLife 5:e14997.

Chevaleyre V, Siegelbaum SA. 2010. Strong CA2 pyramidal neuron synapses define a powerful disynaptic cortico-hippocampal loop. Neuron 66:560–572.

Csicsvari J, Hirase H, Czurko A, Buzsaki G. 1998. Reliability and state dependence of pyramidal cell-interneuron synapses in the hippocampus: An ensemble approach in the behaving rat. Neuron 21: 179–189.

Csicsvari J, Hirase H, Czurko A, Mamiya A, Buzsaki G. 1999. Oscillatory coupling of hippocampal pyramidal cells and interneurons in the behaving Rat. J Neurosci Off J Soc Neurosci 19:274–287.

Danielson NB, Zaremba JD, Kaifosh P, Bowler J, Ladow M, Losonczy A. 2016. Sublayer-specific coding dynamics during spatial navigation and learning in hippocampal area CA1. Neuron 91:652–665.

Deshmukh SS, Knierim JJ. 2011. Representation of non-spatial and spatial information in the lateral entorhinal cortex. Front Behav Neurosci 5:69.

Diba K, Buzsaki G. 2008. Hippocampal network dynamics constrain the time lag between pyramidal cells across modified environments. J Neurosci Off J Soc Neurosci 28:13448–13456.

Dong HW, Swanson LW, Chen L, Fanselow MS, Toga AW. 2009. Genomic-anatomic evidence for distinct functional domains in hippocampal field CA1. Proc Natl Acad Sci USA 106:11794–11799.

Dudek SM, Alexander GM, Farris S. 2016. Rediscovering area CA2: Unique properties and functions. Nat Rev Neurosci 17:89–102.

Eichenbaum H, Dudchenko P, Wood E, Shapiro M, Tanila H. 1999. The hippocampus, memory, and place cells: Is it spatial memory or a memory space? Neuron 23:209–226.

Fernandez-Ruiz A, Makarov VA, Benito N, Herreras O. 2012. Schaffer-specific local field potentials reflect discrete excitatory events at gamma frequency that may fire postsynaptic hippocampal CA1 units. J Neurosci Off J Soc Neurosci 32:5165–5176.

Fernandez-Ruiz A, Munoz S, Sancho M, Makarova J, Makarov VA, Herreras O. 2013. Cytoarchitectonic and dynamic origins of giant positive local field potentials in the dentate gyrus. J Neurosci Off J Soc Neurosci 33:15518–15532.

Fujisawa S, Amarasingham A, Harrison MT, Buzsaki G. 2008. Behavior-dependent short-term assembly dynamics in the medial prefrontal cortex. Nat Neurosci 11:823–833.

Hafting T, Fyhn M, Molden S, Moser MB, Moser EI. 2005. Microstructure of a spatial map in the entorhinal cortex. Nature 436: 801–806.

Hargreaves EL, Rao G, Lee I, Knierim JJ. 2005. Major dissociation between medial and lateral entorhinal input to dorsal hippocampus. Science 308:1792–1794.

Harris KD, Hirase H, Leinekugel X, Henze DA, Buzsaki G. 2001. Temporal interaction between single spikes and complex spike bursts in hippocampal pyramidal cells. Neuron 32:141–149.

Henriksen EJ, Colgin LL, Barnes CA, Witter MP, Moser MB, Moser EI. 2010. Spatial representation along the proximodistal axis of CA1. Neuron 68:127–137.

Hitti FL, Siegelbaum SA. 2014. The hippocampal CA2 region is essential for social memory. Nature 508:88–92.

Huxter J, Burgess N, O'Keefe J. 2003. Independent rate and temporal coding in hippocampal pyramidal cells. Nature 425:828–832.

Igarashi KM, Lu L, Colgin LL, Moser MB, Moser EI. 2014. Coordination of entorhinal-hippocampal ensemble activity during associative learning. Nature 510:143–147.

Ishizuka N, Weber J, Amaral DG. 1990. Organization of intrahippocampal projections originating from CA3 pyramidal cells in the rat. J Comp Neurol 295:580–623.

Ishizuka N, Cowan WM, Amaral DG. 1995. A quantitative analysis of the dendritic organization of pyramidal cells in the rat hippocampus. J Comp Neurol 362:17–45.

Jarsky T, Mady R, Kennedy B, Spruston N. 2008. Distribution of bursting neurons in the CA1 region and the subiculum of the rat hippocampus. J Comp Neurol 506:535–547.

Kadir SN, Goodman DF, Harris KD. 2014. High-dimensional cluster analysis with the masked EM algorithm. Neural Computat 26: 2379–2394.

Kay K, Sosa M, Chung JE, Karlsson MP, Larkin MC, Frank LM. 2016. A hippocampal network for spatial coding during immobility and sleep. Nature 531:185–190.

Kempter R, Leibold C, Buzsaki G, Diba K, Schmidt R. 2012. Quantifying circular-linear associations: Hippocampal phase precession. J Neurosci Methods 207:113–124.

Klausberger T, Somogyi P. 2008. Neuronal diversity and temporal dynamics: The unity of hippocampal circuit operations. Science 321:53–57.

Knierim JJ, Neunuebel JP. 2016. Tracking the flow of hippocampal computation: Pattern separation, pattern completion, and attractor dynamics. Neurobiol Learn Memory 129:38–49.

Kohara K, Pignatelli M, Rivest AJ, Jung HY, Kitamura T, Suh J, Frank D, Kajikawa K, Mise N, Obata Y, Wickersham IR, Tonegawa S. 2014. Cell type-specific genetic and optogenetic tools reveal hippocampal CA2 circuits. Nat Neurosci 17:269–279.

Lee H, Wang C, Deshmukh SS, Knierim JJ. 2015. Neural population evidence of functional heterogeneity along the CA3 transverse axis: Pattern completion versus pattern separation. Neuron 87:1093–1105.

Lee I, Rao G, Knierim JJ. 2004a. A double dissociation between hippocampal subfields: Differential time course of CA3 and CA1 place cells for processing changed environments. Neuron 42:803–815.

Lee I, Yoganarasimha D, Rao G, Knierim JJ. 2004b. Comparison of population coherence of place cells in hippocampal subfields CA1 and CA3. Nature 430:456–459.

Lein ES, Callaway EM, Albright TD, Gage FH. 2005. Redefining the boundaries of the hippocampal CA2 subfield in the mouse using gene expression and 3-dimensional reconstruction. Comp Neurol 485:1–10.

Leutgeb S, Leutgeb JK. 2007. Pattern separation, pattern completion, and new neuronal codes within a continuous CA3 map. Learn Mem 14:745–757.

Leutgeb S, Leutgeb JK, Treves A, Moser MB, Moser EI. 2004. Distinct ensemble codes in hippocampal areas CA3 and CA1. Science 305:1295–1298.

Li XG, Somogyi P, Ylinen A, Buzsaki G. 1994. The hippocampal CA3 network: An in vivo intracellular labeling study. J Comp Neurol 339:181–208.

Lorente de Nó R. 1947. A study of nerve physiology. Studies from the Rockefeller institute for medical research Reprints Rockefeller Institute for Medical Research 131:1–496.

Lu L, Igarashi KM, Witter MP, Moser EI, Moser MB. 2015. Topography of place maps along the CA3-to-CA2 axis of the hippocampus. Neuron 87:1078–1092.

Mankin EA, Diehl GW, Sparks FT, Leutgeb S, Leutgeb JK. 2015. Hippocampal CA2 activity patterns change over time to a larger extent than between spatial contexts. Neuron 85:190–201.

McNaughton BL, Barnes CA, Gerrard JL, Gothard K, Jung MW, Knierim JJ, Kudrimoti H, Qin Y, Skaggs WE, Suster M, Weaver KL. 1996. Deciphering the hippocampal polyglot: The hippocampus as a path integration system. J Exp Biol 199:173–185.

McNaughton N, Morris RG. 1987. Chlordiazepoxide, an anxiolytic benzodiazepine, impairs place navigation in rats. Behav Brain Res 24:39–46.

Mizuseki K, Diba K, Pastalkova E, Buzsaki G. 2011. Hippocampal CA1 pyramidal cells form functionally distinct sublayers. Nat Neurosci 14:1174–1181.

Mizuseki K, Royer S, Diba K, Buzsaki G. 2012. Activity dynamics and behavioral correlates of CA3 and CA1 hippocampal pyramidal neurons. Hippocampus 22:1659–1680.

Mizuseki K, Sirota A, Pastalkova E, Buzsaki G. 2009. Theta oscillations provide temporal windows for local circuit computation in the entorhinal-hippocampal loop. Neuron 64:267–280.

Montgomery SM, Betancur MI, Buzsaki G. 2009. Behavior-dependent coordination of multiple theta dipoles in the hippocampus. J Neurosci Off J Soc Neurosci 29:1381–1394.

Naber PA, Lopes da Silva FH, Witter MP. 2001. Reciprocal connections between the entorhinal cortex and hippocampal fields CA1 and the subiculum are in register with the projections from CA1 to the subiculum. Hippocampus 11:99–104.

Neunuebel JP, Knierim JJ. 2014. CA3 retrieves coherent representations from degraded input: direct evidence for CA3 pattern completion and dentate gyrus pattern separation. Neuron 81:416–427.

O'Keefe J, Dostrovsky J. 1971. The hippocampus as a spatial map. Preliminary evidence from unit activity in the freely-moving rat. Brain Res 34:171–175.

O'Keefe J, Recce ML. 1993. Phase relationship between hippocampal place units and the EEG theta rhythm. Hippocampus 3:317–330.

Oliva A, Fernandez-Ruiz A, Buzsaki G, Berenyi A. 2016. Role of hippocampal CA2 region in triggering sharp-wave ripples. Neuron 91: 1342–1355.

Rolls ET, Kesner RP. 2006. A computational theory of hippocampal function, and empirical tests of the theory. Progr Neurobiol 79:1–48.

Rossant C, Kadir SN, Goodman DFM, Schulman J, Belluscio M, Buzsaki G, Harris KD. 2015. Spike sorting for large, dense electrode arrays. bioRxiv.

Royer S, Sirota A, Patel J, Buzsaki G. 2010. Distinct representations and theta dynamics in dorsal and ventral hippocampus. J Neurosci Off J Soc Neurosci 30:1777–1787.

Schomburg EW, Fernandez-Ruiz A, Mizuseki K, Berenyi A, Anastassiou CA, Koch C, Buzsaki G. 2014. Theta phase segregation of input-specific gamma patterns in entorhinal-hippocampal networks. Neuron 84:470–485.

Sirota A, Montgomery S, Fujisawa S, Isomura Y, Zugaro M, Buzsaki G. 2008. Entrainment of neocortical neurons and gamma oscillations by the hippocampal theta rhythm. Neuron 60:683–697.

Skaggs WE, McNaughton BL, Wilson MA, Barnes CA. 1996. Theta phase precession in hippocampal neuronal populations and the compression of temporal sequences. Hippocampus 6:149–172.

Spruston N. 2008. Pyramidal neurons: Dendritic structure and synaptic integration. Nat Rev Neurosci 9:206–221.

Spruston N, Jonas P, Sakmann B. 1995a. Dendritic glutamate receptor channels in rat hippocampal CA3 and CA1 pyramidal neurons. J Physiol 482:325–352.

Spruston N, Schiller Y, Stuart G, Sakmann B. 1995b. Activity-dependent action potential invasion and calcium influx into hippocampal CA1 dendrites. Science 268:297–300.

Squire LR. 1992. Memory and the hippocampus: A synthesis from findings with rats, monkeys, and humans. Psychol Rev 99:195–231.
Stark E, Roux L, Eichler R, Senzai Y, Royer S, Buzsaki G. 2014. Pyramidal cell-interneuron interactions underlie hippocampal ripple oscillations. Neuron 83:467–480.
Tamamaki N, Abe K, Nojyo Y. 1988. Three-dimensional analysis of the whole axonal arbors originating from single CA2 pyramidal neurons in the rat hippocampus with the aid of a computer graphic technique. Brain Res 452:255–272.
Thompson CL, Pathak SD, Jeromin A, Ng LL, MacPherson CR, Mortrud MT, Cusick A, Riley ZL, Sunkin SM, Bernard A, Puchalski RB, Gage FH, Jones AR, Bajic VB, Hawrylycz MJ, Lein ES. 2008. Genomic anatomy of the hippocampus. Neuron 60: 1010–1021.
Traub RD, Wong RK. 1982. Cellular mechanism of neuronal synchronization in epilepsy. Science 216:745–747.
Valero M, Cid E, Averkin RG, Aguilar J, Sanchez-Aguilera A, Viney TJ, Gomez-Dominguez D, Bellistri E, de la Prida LM. 2015. Determinants of different deep and superficial CA1 pyramidal cell dynamics during sharp-wave ripples. Nat Neurosci 18:1281–1290.
Vinogradova OS. 2001. Hippocampus as comparator: Role of the two input and two output systems of the hippocampus in selection and registration of information. Hippocampus 11:578–598.
Wallenstein GV, Eichenbaum H, Hasselmo ME. 1998. The hippocampus as an associator of discontiguous events. Trends Neurosci 21:317–323.
Witter MP, Wouterlood FG, Naber PA, Van Haeften T. 2000. Anatomical organization of the parahippocampal-hippocampal network. Ann N Y Acad Sci 911:1–24.
Wong RK, Traub RD, Miles R. 1986. Cellular basis of neuronal synchrony in epilepsy. Adv Neurol 44:583–592.
Ylinen A, Bragin A, Nadasdy Z, Jando G, Szabo I, Sik A, Buzsaki G. 1995. Sharp wave-associated high-frequency oscillation (200 Hz) in the intact hippocampus: Network and intracellular mechanisms. J Neurosci Off J Soc Neurosci 15:30–46.